

# Spike-Nosed Projectiles: Computations and Dual Flow Modes in Supersonic Flight

Ameer G. Mikhail\*

U.S. Army Ballistic Research Laboratory, LABCOM, Aberdeen Proving Ground, Maryland 21005

This study was made to assess the capability of a computational fluid dynamic (CFD) method in adequately determining the aerodynamics coefficients for the unusual configurations of sharp-edged spike-nosed projectiles that are of interest to the U.S. Army. McCormack's time-dependent explicit scheme was used for the full Navier-Stokes equations, together with zonal gridding and overlapping approach. Three configurations were computed at Mach = 1.72 and zero incidence angle. The results are compared against wind-tunnel data. The flowfields computed are in agreement with wind-tunnel schlieren photographs, and the computed drag coefficients are within 2% of the wind-tunnel measurements. Two important issues are faced. First is the always existing possibility of a dual flow mode and which one is to occur under specific flow conditions. The second issue is the observed role of the turbulence level and numerical model in affecting the flow separation, and, thus, influencing a particular flow mode to numerically occur. This study demonstrates the successful applicability of the present approach to these untypical configurations and, thus, encourages further application to even more complex spike-nosed configurations, such as those with booms and fins.

## Nomenclature

- $A_{ref}$  = reference area,  $\pi d^2/4$   
 $C_D$  = drag coefficient, drag force/( $0.5 \rho_\infty V_\infty^2 A_{ref}$ )  
 $C_p$  = specific heat under constant pressure  
 $C_v$  = specific heat under constant volume  
 $d$  = reference diameter, in.  
 $d_s$  = spike diameter, in.  
 $e$  = specific total energy  
 $M$  = Mach number  
 $p$  = static pressure, psi  
 $Re$  = Reynolds number  
 $u, v$  = velocity components in the  $x, y$  directions, ft/s  
 $V_\infty$  = freestream velocity, ft/s  
 $x, y$  = Cartesian coordinates for two-dimensional case, axial and radial coordinates for axisymmetric case  
 $\alpha$  = angle of attack, deg  
 $\gamma$  = ratio of specific heats for air  
 $\rho$  = density, slug/ft<sup>3</sup>  
 $\mu$  = laminar (molecular) viscosity coefficient, lb · s/ft<sup>2</sup>  
 $\epsilon$  = turbulent eddy viscosity coefficient, lb · s/ft<sup>2</sup>  
 $\xi, \eta$  = transformed coordinates in the computational plane for the coordinates  $x, y$

## Subscripts

- 0 = denotes stagnation (total) condition  
 $\infty$  = freestream condition

## Introduction

**S**PIKE-NOSED configurations are used for projectile applications against armored targets where the spike is used as a stand-off distance, causing microseconds of advance time between the time that the tip of the spike touches the armor and the time that the warhead (usually a shaped charge) detonates. Spike-nosed configurations are also used for a different

purpose, namely reducing the drag for blunt re-entry vehicles at hypersonic speeds when drag and heating are of a major concern.

After World War II, a new generation of spike-nosed high-explosive antitank (HEAT) projectiles was developed in the U.S. and abroad. In the very early stages of development, during the late 1940s and early 1950s, spinning HEAT projectiles were examined, but it was quickly found that spin reduces the depth of penetration in the armor. Therefore, most spike-nosed projectiles, in the late 1950s and thereafter, were fin-stabilized and were provided with a tail boom and fins behind the shaped-charge warhead.

Many experimental studies were made for finned spike-nosed projectiles. Some wind-tunnel tests can be found, for example, in Refs. 1-5. Some firing range tests are reported in Refs. 6-9. The U.S. Air Force, during the 1960-70s, extensively studied the unsteady front-shock flow phenomenon (the buzzing) for spike-nosed re-entry vehicles at high speeds.<sup>10-12</sup> Also, the Air Force successfully computed the unsteady buzzing flow for these re-entry configurations of interest.<sup>13-15</sup>

At present, for sharp-edged spike-nosed projectiles of interest to the Army, there is no analytic or formal computational procedures that can be systematically used to predict the aerodynamics of such configurations. The Army has relied so far on direct wind-tunnel tests, followed by live firing of projectiles in the firing ranges. The present study was made to establish such a systematic numerical predictive technique. Therefore, validation of the predictive technique against range or wind-tunnel data is of vital importance for assessing the numerical capability. Although the final objective is the application to finned spike-nosed projectiles, this study, being a first step toward that goal, limited itself to unfinned spike-nosed configurations in an attempt to focus on the spike-nosed flow with its complex features. These features include dual flow modes, large separation regions, and unsteadiness. By establishing that such flows can be systematically and successfully computed, the doors will be opened for future work to tackle similar configurations with added booms and fins.

The advances in the zonal gridding and overlapping techniques made this study possible for the present sharp-edged configurations. This represents the first known application of computational fluid dynamics to Army spike-nosed projectile shapes.

Presented as Paper 89-1820 at the AIAA 20th Fluid Dynamics, Plasma Dynamics and Lasers Conference, Buffalo, NY, June 12-14, 1989; received Nov. 27, 1989; revision received Oct. 15, 1990; accepted for publication Oct. 16, 1990. This paper is declared a work of the U.S. Government and is not subject to copyright protection in the United States.

\*Aerospace Engineer, Launch and Flight Division. Senior Member AIAA.

### Test Cases

Very few experimental results are available for unfinned spike-nosed projectiles in contrast to those of finned ones for the reason stated earlier. For the sharp-edged configuration, only the wind-tunnel tests of Platou<sup>16</sup> are applicable. Also, some firing range data are available, but for configurations with a tripping ring.<sup>17</sup> Very recent wind-tunnel tests were made by Koenig et al.,<sup>18</sup> while this work was being completed, for very similar configurations with different spike lengths at Mach numbers between 0.8 to 1.5 and zero angle of incidence. Results of Ref. 18 could be used for further validations in the future.

Three cases from Ref. 16 were chosen. They are shown in Figs. 1-3. The wind-tunnel tests were made in 1950 at the Ballistic Research Laboratory supersonic wind tunnel at  $M = 1.72$  for angles  $-10 \text{ deg} < \alpha < 10 \text{ deg}$ . The Reynolds number was  $4.8 \times 10^6$  per foot,  $T_0 = 100^\circ\text{F}$ , and  $P_0 = 1.26$  atm. The model diameter is 2.5 in. for all three configurations. The first two configurations were reported not to have dual flow modes at this Mach number and range of  $\alpha$ . The flow features of both modes are depicted in Fig. 4. The third configuration was reported to have had the dual flow modes (the high-drag open-flow mode and the low-drag, closed-flow mode). However, the low-drag mode briefly occurred while increasing  $\alpha$  and was captured on a schlieren photograph, but the drag force itself was not measured. The high-drag mode then persisted, whereas the lower drag mode could never be recovered again during the tests.<sup>16</sup>

### Governing Equations

The compressible turbulent Navier-Stokes equations for axisymmetric and two-dimensional flow can be expressed<sup>19</sup> in the following strong conservation form, in which the depen-

dent variables  $\rho, u, v$ , and  $e$  are mass averaged, with  $e$  being the specific total energy,  $T$  being the temperature,  $\rho$  and  $p$  being mean density and pressure, respectively, and  $t$  denoting time:

$$\frac{\partial Q'}{\partial t} + \frac{\partial E'}{\partial x} + \frac{\partial F'}{\partial y} + \left( \frac{F'}{y} + \frac{H'}{y} \right) \beta = 0 \quad (1a)$$

where

$$Q' = \begin{bmatrix} \rho \\ \rho u \\ \rho v \\ \rho e \end{bmatrix} \quad E' = \begin{bmatrix} \rho u \\ \rho u u + \rho - \tau_{xx} \\ \rho u v - \tau_{xy} \\ (\rho e + p)u - \tau_{xx}u - \tau_{xy}v + \dot{q}_x \end{bmatrix}$$

$$F' = \begin{bmatrix} \rho v \\ \rho u v - \tau_{xy} \\ \rho v v + p - T_{yy} \\ (\rho e + p)v - \tau_{xy}u - \tau_{yy}v + \dot{q}_y \end{bmatrix} \quad H' = \begin{bmatrix} 0 \\ 0 \\ -p + \sigma_+ \\ 0 \end{bmatrix}$$

$$\tau_{xx} = -\frac{2}{3}(\mu + \epsilon) \nabla \cdot V + 2(\mu + \epsilon) \frac{\partial u}{\partial x}$$

$$\tau_{xy} = (\mu + \epsilon) \left( \frac{\partial u}{\partial y} + \frac{\partial v}{\partial x} \right)$$

$$\tau_{yy} = -\frac{2}{3}(\mu + \epsilon) \nabla \cdot V + 2(\mu + \epsilon) \frac{\partial v}{\partial y}$$

$$\tau_{\theta\theta} = \sigma_+ = -\frac{2}{3}(\mu + \epsilon) \nabla \cdot V + 2(\mu + \epsilon) \frac{v}{y}$$

$$\nabla \cdot V = \frac{\partial u}{\partial x} + \frac{\partial v}{\partial y} + \left( \frac{v}{y} \right) \beta$$

$$\dot{q}_x = -C_p \left( \frac{\mu}{Pr} + \frac{\epsilon}{Pr_t} \right) \frac{\partial T}{\partial x}$$

$$\dot{q}_y = -C_p \left( \frac{\mu}{Pr} + \frac{\epsilon}{Pr_t} \right) \frac{\partial T}{\partial y} \quad (1b)$$

where  $\mu$  is molecular viscosity,  $\epsilon$  is the turbulent eddy viscosity, and  $\beta = 1$  or 0 for axisymmetric and two-dimensional cases, respectively.

The air is assumed to be a perfect gas, satisfying the equation of state  $p = \rho RT$ , where  $R$  is the gas constant. For the dependence of laminar viscosity on temperature, Sutherland's law was used:

$$\mu = 2.270 \frac{T^{3/2}}{T + 198.6} \times 10^{-8} \text{ lb-s/ft}^2 \quad (2)$$

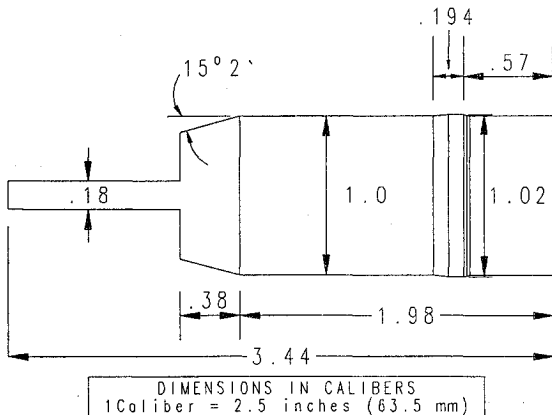


Fig. 1 Wind-tunnel model of the first projectile configuration.

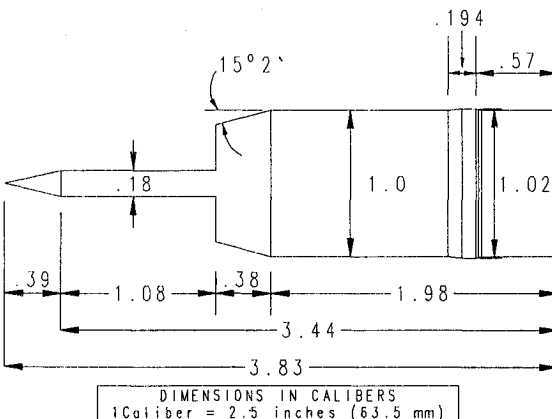


Fig. 2 Wind-tunnel model of the second projectile configuration.

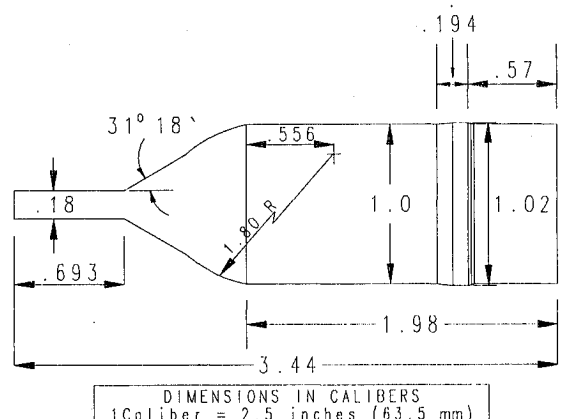


Fig. 3 Wind-tunnel model of the third projectile configuration.

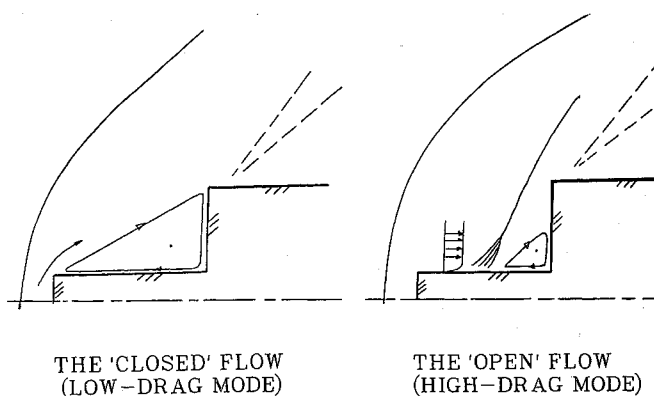


Fig. 4 Typical flow features for the low- and high-drag modes.

The laminar and turbulent Prandtl numbers,  $Pr$  and  $Pr_t$ , were assumed constant with values of 0.72 and 0.9, respectively. The ratio of specific heats  $\gamma$  was also assumed constant and equal to 1.4. The total energy per unit mass,  $e$ , is given by

$$e = C_v T + (\frac{1}{2})(u^2 + v^2)$$

In the  $\xi - \eta$  computational plane, Eqs. (1a) and (1b) are transformed to the conservation law form; the equations can be found, for example, in Ref. 19.

#### Turbulence Model

Turbulence is modeled through the algebraic eddy-viscosity model of Baldwin and Lomax.<sup>20</sup>

Due to the perpendicular surfaces of the spike surfaces at the nose tip and at the facing shoulder, the normal distance to the wall  $y$  is difficult to assign.<sup>21</sup> The problem was solved in Ref. 21 by measuring the  $y$  along a 45-deg ray emanating from the point of intersection of the two perpendicular walls.

### Code, Grid, and Computations

#### Code

The code was developed by Patel and Sturek.<sup>19</sup> It utilizes the familiar and robust explicit time-dependent method of McCormack. The code was vectorized and is run on a Cray-XMP/48 Machine. The present computations were all run in serial arithmetic mode. The zonal grid and overlap provided in the code are represented by eight different available zones (which can be increased if so desired). The user prescribes the overlap between regions along one line of adjacent zones (interface). A global uniform time step was used herein against grid-varying time steps to simulate time-accurate solutions. The time step is determined from the Courant-Fredrick-Levy (CFL) condition, with a factor of 0.6 being used as the Courant number.

#### Boundary Conditions

No-slip conditions are specified on all wall surfaces. The incoming flow conditions are assumed to be of uniform profiles with freestream temperature of  $T_\infty = 520^\circ\text{R}$ ,  $p_\infty = 14.7$  psi,  $M_\infty = 1.72$ .

The outgoing conditions at the end of the projectile were imposed as zero gradients parallel to the body axis direction.

The outer boundary conditions were imposed as nonreflective conditions, i.e., zero-gradient conditions along characteristic lines for all variables. The characteristic direction is determined from the local velocity and temperature. The approach allows setting the "outer" field close to the body without the penalty of any unnecessary approximations regarding shock reflection, or zero-gradient conditions.

At the symmetry line, ahead of the spike tip, a two-point zero-gradient boundary condition is imposed on the solved variables.

#### Initial Conditions

Computations were started using freestream values everywhere in the domain. These values are for freestream velocity, pressure, and temperature. The density and specific total energy are computed accordingly, using the equation of state and the definition of the specific total energy.

#### Grid

Three different grid zones were used in the computation. Those zones and the extent of the computational domain are depicted in Fig. 5.

For the first configuration, the grids used for the three zones are  $15 \times 48$ ,  $26 \times 39$ , and  $21 \times 25$ , respectively. The first and second arguments in the parentheses refer to the axial and radial directions, respectively. This grid has 2259 total points and is equivalent to a  $48 \times 48$  grid.

One restriction in the present grid overlapping technique is the requirement that no interpolation is allowed at the interface line between zones. Thus, each point on either side of any two zones must have exactly the same coordinates. This restriction represents some constraint in the flexibility of the grid distribution and may be alleviated in future development of the code. Meanwhile, to accommodate this restriction, one has to accept unnecessary clustering of points in some locations. Figure 6 shows the clustered points along lines parallel to the top body surface, where clustering is needed near the body to resolve the turbulent boundary layer. Figure 6 shows the overall grid distribution for the first projectile configuration.

The sharp cone spike configuration was also modeled using three zones, but with grid sizes of  $15 \times 39$ ,  $26 \times 39$ , and  $21 \times 25$ , respectively. This grid totals 2124 points, or the equivalent of a  $46 \times 46$  mesh, and is depicted in Fig. 7.

The third configuration was computed using zones of sizes  $15 \times 44$ ,  $21 \times 35$ , and  $31 \times 35$ . The grid totals 2480 points or  $50 \times 50$ , approximately. This grid for configuration 3 is given in Fig. 8. The grids were generated using a simple algebraic (exponential) formula in each zone in both the axial and radial directions.

### Results

#### Configuration 1

The low-drag mode was obtained by straightforward computation, assuming the flow to be fully turbulent everywhere. Unsteadiness occurred in the computation, but, when the turbulence level was reduced to 0.2 of its value at each point, the flow became steady. The Mach contours are provided in Fig. 9. Comparison with the schlieren photograph of Ref. 16 indicated good agreement of flow features. The bow shock stand-off distance was  $0.5d_s$ , as theoretically predicted, and the bow shock angle away from the body nose tip was about 40 deg, the same as can be determined from the schlieren. The computations converged satisfactorily after 4000 time steps,

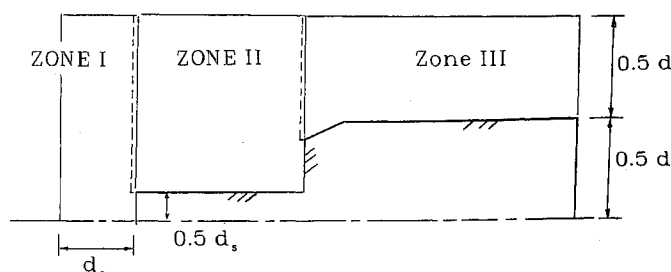


Fig. 5 Grid zones and computational domain for the spike-nosed projectiles.

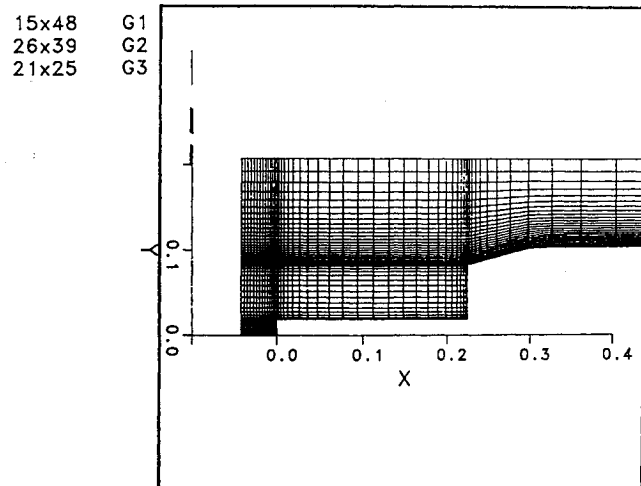


Fig. 6 Zonal grid for the first projectile configuration.

1.72  $M_\infty$   
 0.00°  $\alpha$   
 $3.61 \times 10^6$  Re  
 15x48 G1  
 26x39 G2  
 21x25 G3

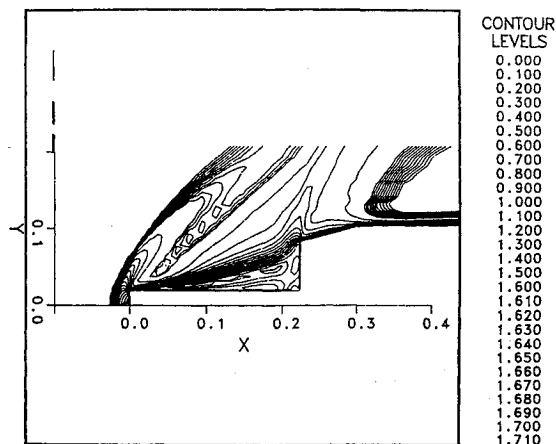


Fig. 9 Mach number contours for the low-drag mode for configuration 1.

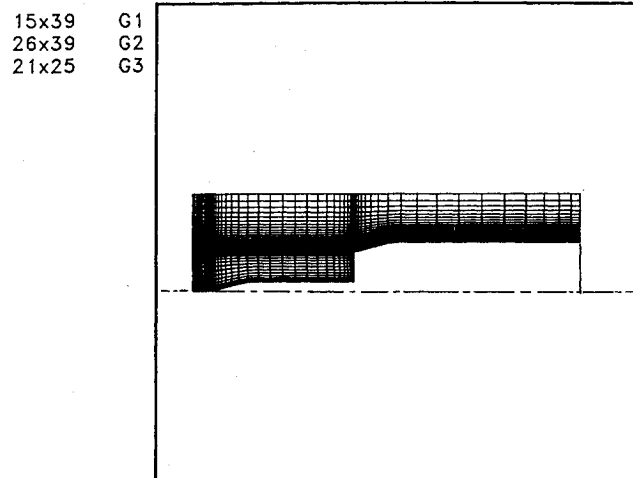


Fig. 7 Zonal grid for the second projectile configuration.

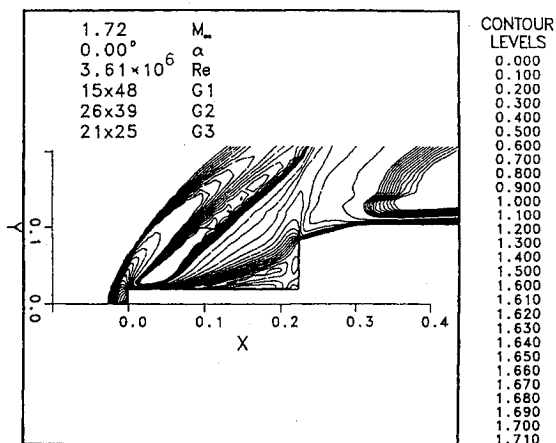


Fig. 10 Mach number contours for the high-drag mode for configuration 1.

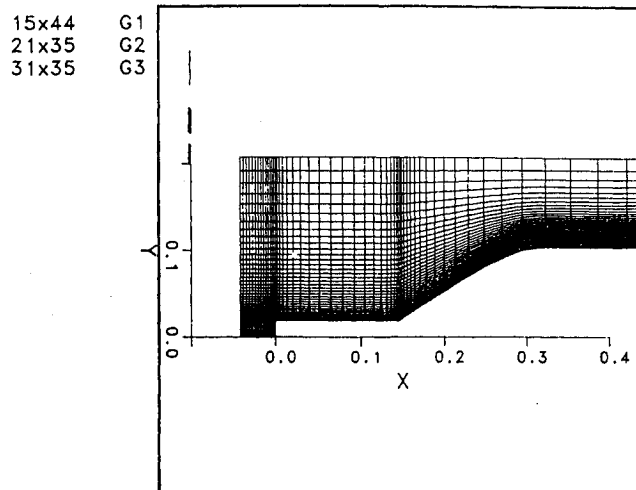


Fig. 8 Zonal grid for the third projectile configuration.

1.72  $M_\infty$   
 0.00°  $\alpha$   
 $3.61 \times 10^6$  Re  
 15x48 G1  
 26x39 G2  
 21x25 G3

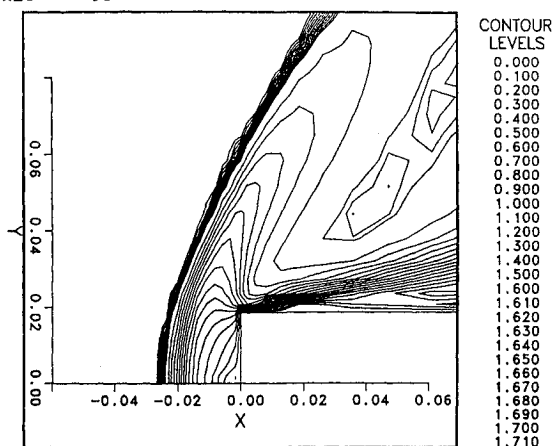


Fig. 11 Details of Mach number contours near the spike tip (low-drag, configuration 1).

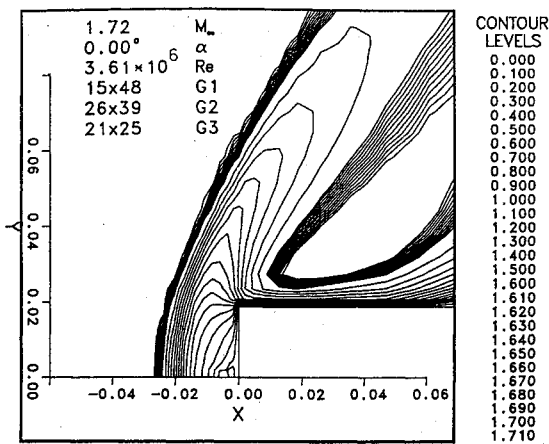


Fig. 12 Details of Mach number contours near the spike tip (high-drag, configuration 1).

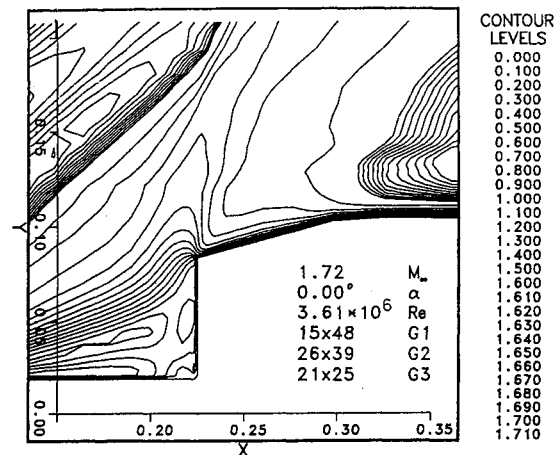


Fig. 14 Details of Mach number contours near the facing shoulder (high-drag, configuration 1).

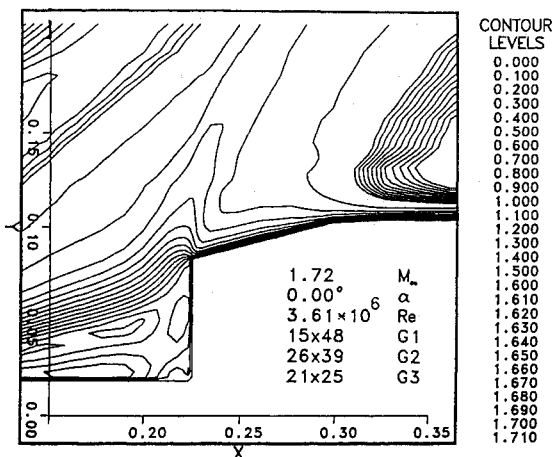


Fig. 13 Details of Mach number contours near the facing shoulder (low-drag, configuration 1).

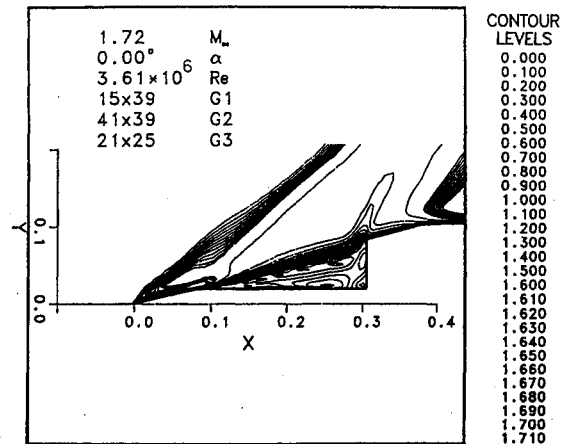


Fig. 15 Mach number contours for configuration 2 (low-drag mode).

although the code was later run to 12,000 steps to assure the stability of the computations. The computer CPU time was 40 min on the Cray-XMP/48 for the 4000 steps.

Several numerical experiments were made to obtain the high-drag mode, even though that mode was not confirmed during the tests of Ref. 16. The high-drag mode was easily obtained by freezing (i.e., not updating) the turbulence level after 1000 steps and by simultaneously relaxing the time step at each point to 0.6 of its local Courant time step value. The solution also converged satisfactorily after 6000 time steps, using 60 minutes on the same computer. Figure 10 depicts the flowfield, as presented by the Mach contours for this high-drag mode.

Comparison between the local flowfields of the two modes near the spike tip is given in Figs. 11 and 12, respectively. For the high-drag mode, there is an expansion fan near the tip, which is followed immediately by coalescence of compression waves facing the separation region. These compression waves coalesce into a shock that faces the facing shoulder of the projectile, thus raising the pressure behind it and also that on the facing wall. This higher pressure results in the higher drag of the projectile. Surprisingly, the corresponding flow detail near the facing shoulder differs very slightly for the two modes. It was expected that larger differences would be observed there. Figures 13 and 14 provide the details for those modes near the facing shoulder.

The forebody drag coefficient for the computed geometry (low-drag) was 0.337. The drag due to the rotating band, which is shown in Figs. 1-3 but was not modeled in the

computation, was estimated<sup>22</sup> to be 2% of the total drag at  $M = 1.72$ . The computed drag is, therefore, provided as 0.344; the wind-tunnel measurement given in Ref. 16 is 0.351 for the forebody drag. Reference 16 provides the net forebody drag without any reference to base drag corrections. The computation, thus, underpredicts the measurement by 2%. Considering the tunnel measurement accuracy, one can conclude that these flow results are very assuring and useful. For the high-drag mode, the computed drag coefficient was 0.402 and is provided as 0.410 when including the 2% rotating band effect. The high-drag mode, therefore, resulted in a 19% increase in drag over the low-drag mode.

#### Configuration 2

The high-drag mode was obtained first when the computation of configuration 1 was repeated, assuming fully turbulent flow everywhere and no reduction in the turbulence level. The computation was slower in converging, requiring 7000 time steps for satisfactory convergence.

To obtain the low-drag mode, which is the mode reported<sup>16</sup> to occur, laminar flow and transition should be allowed to occur on the cone. Therefore, laminar flow was allowed on the cone, and transition was allowed to occur only along the middle third of the whole spike length. This was based on estimates of location of transition (local Reynolds number), which were evaluated using Refs. 23 and 24. The low-drag mode was immediately obtained, but with slower convergence rate. Convergence required about 12,000 time steps, requiring 120 min on the Cray-XMP/48 Machine.

The two flow modes are depicted in Figs. 15 and 16. In Fig. 15, the flow seems to slide over the separated region of the spike, whereas in Fig. 16, for the high-drag mode, there is a compression wave appearing at the beginning of the separated region, thus signifying flow path turning.

The forebody drag coefficient for the low-drag case was 0.314 (including the 2% rotating band drag), compared to 0.321 for the wind-tunnel measurement. Again, computation is within 2% of the measurement. The high-drag mode drag

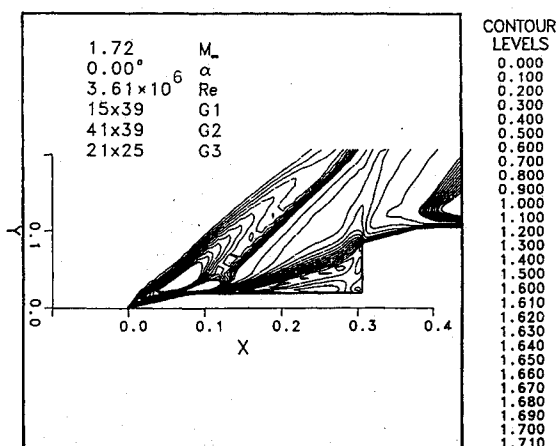


Fig. 16 Mach number contours for configuration 2 (high-drag mode).

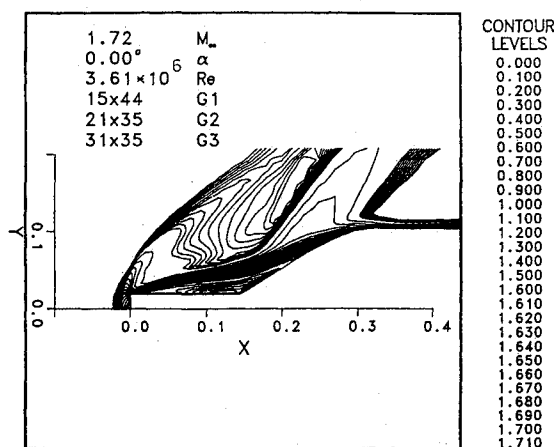


Fig. 17 Mach number contours for configuration 3 (low-drag mode).

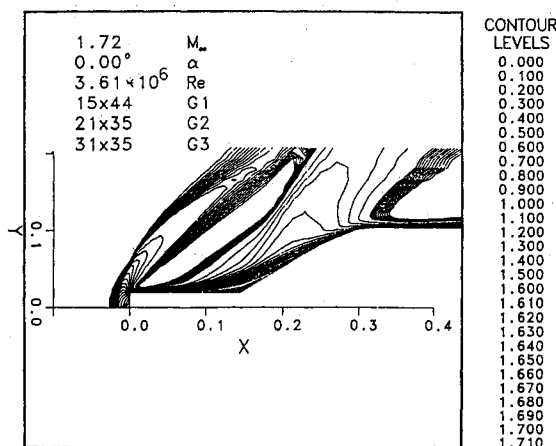


Fig. 18 Mach number contours for configuration 3 (high-drag mode).

coefficient was computed as 0.397 (including the 2%) and, thus, is 26% higher than that of the low-drag mode. The high drag was not observed during the tests of Ref. 16.

### Configuration 3

The high-drag mode was obtained readily when the computation, similar to that for configuration 1, was applied here. Fully turbulent flow everywhere with no reduction in turbulence level was applied. Computations required only 4000 steps for satisfactory convergence.

Several numerical attempts were made to obtain the low-drag mode. It was found that, by imposing a 3.5% crossflow (i.e.,  $v = 0.035 V_\infty$ ) in the freestream in zone 1, the flow mode was readily obtained. This 3.5% crossflow falsely simulated a pseudo 2-deg angle of attack. Although this is not truly an angle-of-attack effect, the cross velocity is an influence that can be related to an angle of attack.

These flowfields are depicted in Figs. 17 and 18 for low-drag and high-drag modes, respectively. An excellent agreement for the high-drag mode was obtained with the schlieren photograph of Ref. 16. One feature is the existence of a "kink" in the compression wave, which emanates from the impact of the flow with the separation region. This kink was questioned at first, but, when the schlieren photo had been examined carefully, the kink was found easily. Also, all the shock and expansion wave angles (away from the body) were found to be within 4 deg for the values measured from the schlieren photograph of Ref. 16.

The forebody drag coefficient for the high-drag mode was computed as 0.478 (including the 2% increase due to the rotating band) compared to 0.306 for the low-drag case. This represents a 56% increase in drag. The wind-tunnel measurement for the high-drag mode was reported<sup>16</sup> to be 0.555. This large discrepancy between the computed and measured values is still unresolved. However, when examining this particular case in Ref. 16, the value of 0.555 seems to be particularly high in comparison with the remaining cases tested. The data of Ref. 16 for this case were presented with only one point on one figure in the report. There are no crosschecked values or any tabulated results for positive verification of this value. Table 1 provides a summary of all obtained results and a comparison with the test data.

### Grid Size Effect

To examine the result obtained for the high-drag mode for configuration 3, the computations were performed again using a larger number of points to assess whether that discrepancy was due to inadequate grid size. Configuration 3 was computed first using zones with  $15 \times 44$ ,  $21 \times 35$ , and  $31 \times 35$  points. This grid totals 2480 points, with a  $50 \times 50$  mesh equivalence. The grid was then increased to  $15 \times 54$ ,  $31 \times 45$ , and  $41 \times 45$ , thus totalling 4050 points, which is equivalent to a  $63 \times 63$  mesh. The drag coefficient changed from 0.4621 to 0.4690, a change of only 1.5%. Therefore, it was assumed that the grid size is appropriate for most purposes.

Table 1 Comparison of results at Mach = 1.72

Configuration	$C_D$			
	Low-drag mode		High-drag mode	
	Wind tunnel	Present computations <sup>a</sup>	Wind tunnel	Present computations <sup>a</sup>
1	0.351	0.344	— <sup>b</sup>	0.410
2	0.321	0.314	— <sup>b</sup>	0.395
3	— <sup>c</sup>	0.306	0.555	0.469

<sup>a</sup>These values include an added 2%, due to rotating band pressure drag<sup>22</sup> at  $M = 1.72$ .

<sup>b</sup>This flow mode was not reported in the wind-tunnel experiment.<sup>16</sup>

<sup>c</sup>This mode was observed and reported only in a schlieren photograph but quickly disappeared and could not be recovered<sup>16</sup> in the wind tunnel for actual measurement.

### Summary and Conclusions

Three different spike-nosed projectile configurations were computed at Mach = 1.72, and the results are compared to wind-tunnel measurements. The computed drag coefficients are in very good agreement with the measured values. Computed values are within 2% of the measurements, which is within the drag-measurement accuracy itself. The high-drag mode computed for the third configuration provided a considerably lower drag than the measured value, although the detailed flow features compared rather accurately with the schlieren photograph of the test. Because confidence was gained from the two previous computed cases, it is believed that the drag measurement for this particular case is quite high and may also be in error. This belief is supported by observing the results of 20 similar spike-nosed configurations tested during the same test period. These drag data are also reported in Ref. 16.

Two interesting obstacles are faced in this study that cannot be resolved decisively. First, the possibility of two flow modes always exists. Therefore, one cannot determine, a priori, which mode the numerical procedure will favor. Also, it is not known, a priori, which one will physically occur at particular wind-tunnel conditions or under free-flight firing range conditions. The second obstacle faced was the strong role of the turbulence eddy viscosity value level and model on influencing the computation (possibly due to the large separation region) toward one particular flow mode. It was not determined whether this influence is purely a numerical problem or if it has a parallel in nature where flow turbulence in the tunnel or in free flight may trigger a particular flow mode.

Finally, this study provided a straightforward and systematic capability for computing such difficult configurations. The present work represents an advance in the application of CFD techniques. The computations, in addition, have provided dual flow modes where the wind-tunnel experiment had only revealed one mode under certain tunnel conditions. It is not known if some of these computed dual modes are superficial or whether real-life tests had favored only one mode that is more dominant. Thus, these computations may spur the need for extensive and delicate variations in test conditions to verify the existence of these modes at these flow conditions.

### Acknowledgment

The help given by N. R. Patel in the early stage of code adoption and initial problem setup is gratefully acknowledged.

### References

- <sup>1</sup>Krieger, R. H., "Wind Tunnel Test of the T153 120mm HEAT Projectile," U.S. Army Ballistic Research Lab., Aberdeen Proving Ground, MD, BRL-TN-724, Aug. 1952.
- <sup>2</sup>Sylvester, M. A., and Krieger, R. H., "Wind Tunnel Tests of the T340E11 90mm HE Projectile with Varying Spike Nose and Spool-Type-Body Parameters," U.S. Army Ballistic Research Lab., Aberdeen Proving Ground, MD, BRL-MR-1146, April 1958.
- <sup>3</sup>Falkowski, E. W., "Static and Dynamic Stability Characteristics of the Supersonic Infantry Projectile at Transonic Velocities," U.S. Army Picatinny Arsenal, Dover, NJ, TM-1565, June 1965.
- <sup>4</sup>Falkowski, E. W., and Fleming, G. C., "Aerodynamic Characteristics of the Modified 105-mm M490 Training Projectile," U.S. Army Armament Research and Development Center, Dover, NJ, ARLCD-TR-81043, April 1982.
- <sup>5</sup>Corce, J. D., and Best, J. T., "Static Stability and Axial Force Characteristics of Several U.S. Army 105-mm Antitank Projectile Configurations at Mach Numbers 1.5 to 3.5," Arnold Air Force Station, TN, AEDC-TR-76-101, Sept. 1976.
- <sup>6</sup>Karpov, B. G., and Piddington, M. J., "Effect on Drag of Two Stable Flow Configurations Over the Nose Spike of the 90mm T316 Projectile," U.S. Army Ballistic Research Lab., Aberdeen Proving Ground, MD, BRL-TN-595, Oct. 1954.
- <sup>7</sup>Krieger, R. H., "The Aerodynamic Design of Fin Stabilized Ammunition," U.S. Army Ballistic Research Lab., Aberdeen Proving Ground, MD, BRL-MR-971, Feb. 1965.
- <sup>8</sup>Sabin, C. P., "The Aerodynamic Properties of a Spike-Nosed Shell at Transonic Velocities," U.S. Army Ballistic Research Lab., Aberdeen Proving Ground, MD, BRL-MR-1112, Nov. 1957.
- <sup>9</sup>McCoy, R. L., "A Limited Aerodynamic Test of the 105mm Projectile, M456A1, and Three Nose-Spike Modifications," U.S. Army Ballistic Research Lab., Aberdeen Proving Ground, MD, ARBRL-MR-02862, Sept. 1978.
- <sup>10</sup>Guenther, R. A., and Reding, P. J., "Fluctuating Pressure Environment of a Drag Reducing Spike," *AIAA Journal*, Vol. 14, Dec. 1977, pp. 705-710.
- <sup>11</sup>Ericsson, L. E., "Flow Pulsation on Concave Conic Forebodies," *Journal of Spacecraft and Rockets*, Vol. 15, Sept.-Oct. 1978, pp. 287-292.
- <sup>12</sup>Reding, P. J., and Jecmen, D. H., "Effects of External Burning on Spike-Induced Separated Flow," *Journal of Spacecraft and Rockets*, Vol. 20, Sept.-Oct. 1983, pp. 452-453.
- <sup>13</sup>Haupt, B. F., and Koenig, K., "Aerodynamic Effects of Probe-Induced Flow Separation on Bluff Bodies at Transonic Mach Numbers," *Journal of Spacecraft and Rockets*, Vol. 24, July-Aug. 1987, pp. 327-333.
- <sup>14</sup>Shang, J. S., Hankey, W. L., and Smith, R. E., "Flow Oscillations of Spike-Tipped Bodies," *AIAA Journal*, Vol. 20, Jan. 1982, pp. 25-26.
- <sup>15</sup>Calarese, W., and Hankey, W. L., "Modes of Shock-Wave Oscillations on Spike-Tipped Bodies," *AIAA Journal*, Vol. 23, Feb. 1985, pp. 185-192.
- <sup>16</sup>Platou, A. S., "Body Nose Shapes for Obtaining High Static Stability," U.S. Army Ballistic Research Lab., Aberdeen Proving Ground, MD, BRL-MR-592, Feb. 1952.
- <sup>17</sup>MacAllister, L. C., unpublished Firing Range Measurements, Launch and Flight Division, U.S. Army Ballistic Research Lab., Aberdeen Proving Ground, MD, 1980.
- <sup>18</sup>Koenig, K., Bridges, D. H., and Chapman, G. T., "Transonic Flow Modes of an Axisymmetric Blunt Body," *AIAA Paper 88-3536*, July 1988.
- <sup>19</sup>Patel, N. R., and Sturek, W. B., "Multi-Tasked Numerical Simulation of Axisymmetric Ramjet Flows Using Zonal, Overlapped Grids," U.S. Army Ballistic Research Lab., Aberdeen Proving Ground, MD, BRL-MR-3834, May 1990.
- <sup>20</sup>Baldwin, B. S., and Lomax, H., "Thin-Layer Approximation and Algebraic Model for Separated Turbulent Flows," *AIAA Paper 78-257*, Jan. 1978.
- <sup>21</sup>Danberg, J. E., and Patel, N. R., "An Algebraic Turbulent Model for Flow Separation Caused by Forward and Backward Facing Steps," U.S. Army Ballistic Research Lab., Aberdeen Proving Ground, MD, BRL-MR-3791, Dec. 1989.
- <sup>22</sup>NSWC-AP Code; Devan, L., and Mason, L. A., "Aerodynamics of Tactical Weapons to Mach 8 and Angle of Attack 180°: Part II, Computer Program and Users Guide," Naval Surface Weapons Center, Dahlgren, VA, NSWC-TR-81-358, Sept. 1981.
- <sup>23</sup>Whitefield, J. D., and Potter, J. L., "The Influence of Slight Leading Edge Bluntness on Boundary-Layer Transition at Mach Number of Eight," Arnold Engineering Development Center, TN, AEDC-TDR-64-18, March 1964.
- <sup>24</sup>Sheetz, N. W., "Ballistics Range Experiments on the Effect of Unit Reynolds Number on Boundary-Layer Transition," *Proceedings of the 8th Navy Symposium on Aeroballistics*, Naval Weapons Center, Corona, CA, May 6-8, 1969, Vol. I, June 1969, pp. 201-214.

Clark H. Lewis  
Associate Editor